Continental Shelf Research 286 (2025) 105421

Contents lists available at ScienceDirect

Continental Shelf Research

journal homepage: www.elsevier.com/locate/csr

Research papers

Wind-driven variability in longshore transport of SPM in the turbidity maximum zone along the Dutch coast

Carola M. van der Hout [a,b], Rob Witbaard [a], Piet Hoekstra [c,d], Theo Gerkema [a,*]

[a] NIOZ Royal Netherlands Institute for Sea Research, Department of Estuarine and Delta Systems, P.O. Box 140, 4400 AC Yerseke, The Netherlands
[b] Rijkswaterstaat, Ministry of Infrastructure and Water Management, P.O. Bos 2232, 3500 GE Utrecht, The Netherlands
[c] Utrecht University, Department of Physical Geography, P.O. Box 80,.115, 3508TC Utrecht, The Netherlands
[d] Waddenacademie, Board of directors Wadden Academy – Geosciences and Climate Portfolio, Ruiterskwartier 121a, 8911 BS Leeuwarden, The Netherlands

ARTICLE INFO

Dataset link: https://doi.org/10.25850/nioz/7b.b.ah

Keywords:
SPM
Transports
Dutch coast
Wind climate
Long-term measurements

ABSTRACT

Long-term measurements from a mooring off the Dutch coast, placed in the turbidity maximum zone (TMZ), are analyzed to study the temporal variability of the alongshore transport of SPM (Suspended Particulate Matter), covering a two-year period. In particular, the effect of wind speed and wind direction is investigated, as it is dominant over the tidal effect. The data reveal that the general net transport at the mooring location is northward; annually, the mean northward transport is 1 kton per meter in the cross-shore direction. For calm conditions, when wind speeds are less than 5 m/s, the overall effect of winds on the net transport diminishes to zero. Energetic conditions (wind speed higher than 5 m/s) are studied for a sequence of storms from opposing wind directions. Here, the gross tidal transports (i.e., transport during ebb or flood separately) show a delay with respect to the onset of the wind event, ranging from half a day to a day. The correlation between the net transport per tidal cycle and the wind characteristics during that cycle, is used to extrapolate the results to a 10-year period, using wind data from a nearby weather station. It is shown that annual transports of SPM can vary by a factor of two between years, due to different wind and wave conditions. Within a year the seasonal variability is larger, a factor of five exists between summer and winter months.

1. Introduction

The main pathways and distribution of Suspended Particulate Matter (SPM) in the southern part of the North Sea were established in recent decades (e.g. Eisma, 1987; van Alphen, 1990; McManus and Prandle, 1997; Dyer and Moffat, 1998; de Kok, 2004; Lafite et al., 2007; Fettweis et al., 2007). Most of the material originates from Dover Strait, while local sources of bank erosion and riverine input act as minor contributors. The SPM transport through Dover Strait splits more or less evenly into two parts, as depicted in Fig. 1: 40% follows the English coast and merges with the East-Anglia plume and 60% follows the Belgian-Dutch coast; the latter is the focus in this study. The two (partially) merge again further north in the German Bight. In this, the Dutch coastal waters act as a transit for the generally northward SPM transport along the continental coast. Part of this SPM budget forms a major source of fine sediments and nutrients for the Wadden Sea system (Colina Alonso et al., 2024), which stretches from the Netherlands to Denmark; it is a UNESCO world heritage area known for its unique natural habitats. Colina Alonso et al. (2024) provide an overview of the present understanding of the sources and sinks of SPM in the basins of the Wadden Sea. Changes in the coastal SPM transport will directly affect this ecosystem. They may come from human interventions in the coastal system and from natural changes. Natural variations are atmospheric variability (on annual to decadal scales) affecting wind-driven transports, or in the long run from climate change via changes in river discharge, sea level and wind climate. Concerning the human interventions – such as harbor works and engineering works – a new trend has started to investigate the possibilities to withdraw mud from harbors instead of relocating it downstream of the harbor. The mud is then processed into products, landfill or dike reinforcements. The local benefit is sought in alleviation of dredging activities by the permanent withdrawal. However, to predict the effect of such changes on the budget of SPM in the Wadden Sea, it is necessary to know the actual budget of SPM towards it, its natural variability and the governing transport processes.

A clear indication of natural variability is already found at the primary source region of Dover Strait. Both the sediment concentration and the direction and magnitude of the water transport through Dover

* Corresponding author at: NIOZ Royal Netherlands Institute for Sea Research, Department of Estuarine and Delta Systems, P.O. Box 140, 4400 AC Yerseke, The Netherlands.
E-mail address: theo.gerkema@nioz.nl (T. Gerkema).

https://doi.org/10.1016/j.csr.2025.105421
Received 7 July 2024; Received in revised form 5 January 2025; Accepted 21 January 2025
Available online 29 January 2025

Strait are sensitive to the wind direction and speed (Prandle, 1978; van Alphen, 1990). This already leads to a range in, e.g., seasonal or annual SPM fluxes. An additional factor is the large uncertainty due to differences in sampling approaches as well as spatial and temporal limitations (Fettweis and van den Eynde, 2003; Fettweis et al., 2007). The estimates for the SPM transport through Dover Strait range between 13 and 45 Mton/yr (McManus and Prandle, 1997; Fettweis and van den Eynde, 2003). Other sources, like the Flemish Banks and the Rhine-Meuse river system, are in the order of 2 Mton/yr each, thus comparatively minor (Fettweis and van den Eynde, 2003; de Kok, 2004; Cox et al., 2021). All in all, an estimated 8–32 Mton/yr of the SPM from Dover Strait passes along the Belgian-Dutch coast (Fettweis et al., 2007). A 3D numerical model study of the Southern North Sea gives an estimate of 12 Mton/yr over a cross-sectional area of 30 km (Cronin and Blaas, 2015), which is at the lower end of the given range.

Along the Dutch coast the SPM remains close to the coastline as indicated by in-situ observations (Visser et al., 1991; Joordens et al., 2001; van der Hout et al., 2015) and as seen from satellite observations (van Raaphorst et al., 1998; Fettweis et al., 2007; Pietrzak et al., 2011), such as the image in Fig. 1. It is the large freshwater discharge of the river Rhine that keeps the SPM attached to the coastline, by forming a cross-shore density gradient along the coast that generally drives an anti-clockwise circulation in the cross-shore direction (van Alphen, 1990; van der Giessen et al., 1990; Visser et al., 1991; de Boer et al., 2008). de Kok (2004) framed these observations in the concept of a sediment river, where SPM is trapped and transported in Northeasterly direction. The near-bed SPM concentrations in the turbidity maximum zone (TMZ) that fringes the coastal zone can reach up to 2 g/l (van der Hout et al., 2017). The observations of the TMZ confirmed definitely the idea that a major part of the SPM may be transported via this turbidity zone. As the TMZ occupies only a relatively small area of the coastal zone, it forms a natural focal area for further studying the residual SPM transport.

In 2011 and 2012 a bottom frame was deployed in the TMZ to monitor the SPM concentrations and the current velocities. The nature of this dataset lends itself to identify processes that drive the alongshore transport of SPM. First of all there is the tidal current. This is a predictable and fairly steady actor and hence no major variability in transport is to be expected as far as this driver is concerned. This stands in contrast to the wind-driven transport, which is highly variable on time scales from days to decades. The impact of wind on the transport of SPM is intermittent and episodic, and its effect comes about in two ways. Firstly, as the southern North Sea is limited in depth, wind-generated waves induce resuspension of sediment (Stanev et al., 2009; van der Hout et al., 2017); secondly, the wind-driven flow forms a transport pattern of its own (Otto et al., 1990). A third and final factor is the density-driven flow at the inner shelf induced by the large fresh water discharge of the river Rhine into the North Sea. The fresh water is deflected northward and pushed towards the coast to form a region of fresh water influence (ROFI). The complex interactions between the three mechanisms near the main river outlet – i.e. in the bulge of the Rhine ROFI – were studied by de Boer et al. (2009). Here, we have chosen to study the resulting transport pattern downstream (thus north) of the Rhine ROFI. There, the alongshore density gradients are weaker (although a marked cross-shore gradient remains present, as shown by Rijnsburger et al. (2016)). This reduces the effect of the density-driven flow on the transport of SPM. Therefore the alongshore density driven processes are not specifically considered in this study. Also because the observations are limited to a single point, the contribution cannot be distinguished from the tidal alongshore process.

To advance our understanding of the drivers of SPM transport along the Dutch coast, the following three processes are addressed here: advection by tidal currents – and implicitly density gradients –, resuspension by waves, and wind-driven flow. Section 2 gives a description of the dataset used for the analysis and a description of the research area and the characteristics of the wind climate at the Dutch

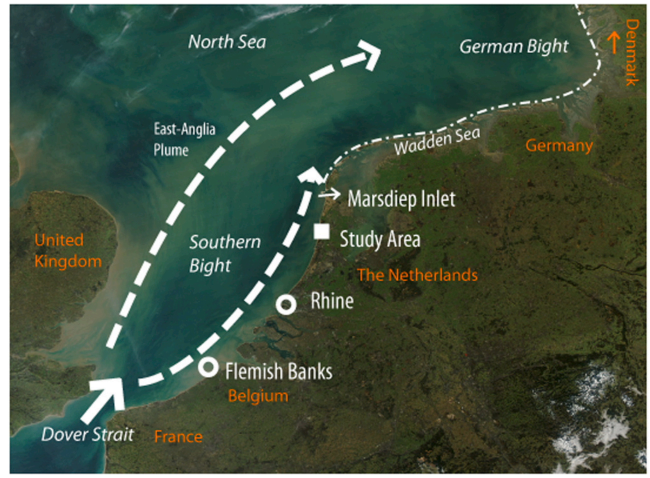

Fig. 1. Satellite image on a cloudless day revealing high surface concentrations in the Southern Bight of the North Sea. The white arrows depict roughly the known overall SPM transport routes and the white circles highlight two further SPM sources along the coast. The study area at the Dutch coast is indicated by the white square. The white dash-dotted line indicates the outer edge of the Wadden Sea islands and inlets (Image source: NASA).

coast. Section 3 focuses on the methods applied to derive SPM transport numbers from the field data. As the focus of this study is on time scales beyond the tidal cycle itself, hence we calculate aggregate quantities to sum up its effects: the gross (ebb and flood) and net transports. This section also describes the method applied for the conversion of the acoustic backscatter of an ADCP to SPM concentrations. We found earlier that at the study site the resuspension of SPM is controlled by the wave height rather than the tidal current (van der Hout et al., 2017). Hence, we expect larger gross transports with higher waves, which is the subject of Section 4. In Section 5 the net transports are analyzed. The large variety of atmospheric conditions in the long-term dataset serves as a suitable basis to analyze the respective advective transports by the wind and the tide. The dataset can be split in calm and energetic conditions on the basis of a wind speed and wave height threshold. During the calm conditions the effect of the wave height and wind speeds on the net transport is found to be negligible. Hence, the tidal current – and implicitly the longshore density processes – part can be assessed. For high-energy conditions, linear relations are established per wind direction between the net SPM transport per tidal cycle and the wind speed. In Section 6, these results are extrapolated to a ten-year period to evaluate the year-average transport and its natural variability. The paper ends with a discussion in Section 7 and a concluding summary in Section 8.

2. Research area and datasets

2.1. Research area

The deployment (52°38.249′N; 4°36.294′E) was located near Egmond, at the Dutch coast in the Southern Bight of the North Sea, 20 km north of the port of IJmuiden, and 80 km North of the Rhine river outflow (Fig. 1). In this area a coastal Turbidity Maximum Zone (TMZ) fringes the coastline, as identified by van der Hout et al. (2015). In the cross-shore direction, in a zone from 0.75 to 2.5 km offshore, SPM concentrations in the TMZ are similar to those at the present bottom frame location (van der Hout et al., 2015); they range from 20 mg/l to 2 g/l. The seabed is sandy with a median grain size of 220 μm, a d50 of 180 μm and a clay percentage of 5% in the top 0.05 m layer (Witbaard et al., 2017). The median grain size of the SPM in the turbidity plume is 10 μm, with an average organic content of 45% (van der Hout et al., 2017).

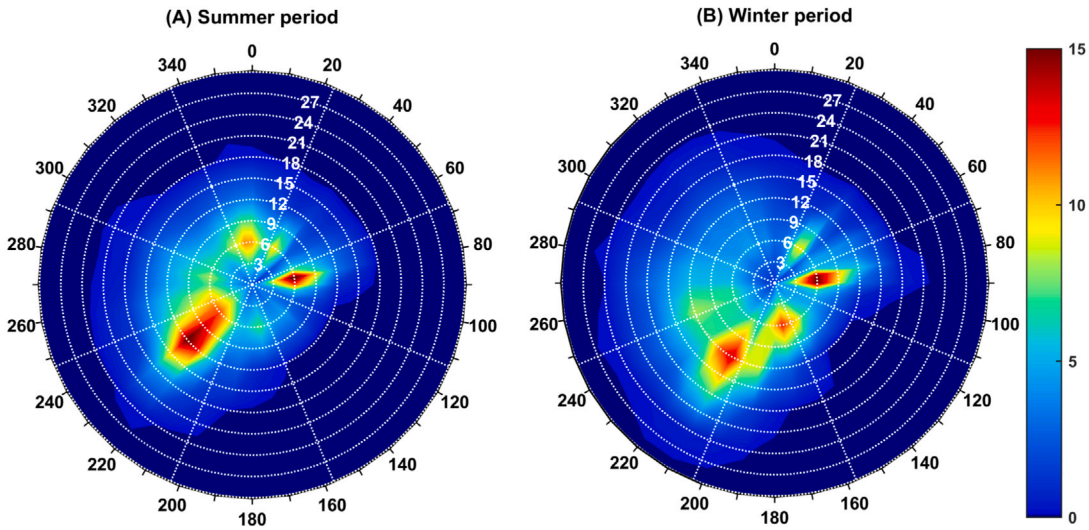

Fig. 2. Wind climate separated in summer period (A; Apr–Sept) and the winter period (B; Oct–Mar) based on the ten-year record (2004–2013) from IJmuiden weather station (source: KNMI). The colors indicate the percentage of observed wind conditions, dark blue marks 0 observations. On the (white) radial axis is the wind speed (w_s) per 3 m/s bins. Percentages are determined per 10 degrees and 1 m/s.

2.2. Wind climate in the southern North Sea

As stated in the 1, the variability in the atmospheric forcing in the North Sea is expected to be a major factor in the net transport of SPM. We here provide a brief description of that variability. We use wind data from the nearby IJmuiden weather station (source: KNMI). The (average) wind climate is dominated by southwesterly and westerly winds and to a lesser extent by northerlies. The northerlies and westerlies are mostly present in the summer period (Apr–Sept), and the southwesterlies predominantly in the winter period (Oct–Mar) (Fig. 2). Siegismund and Schrum (2001) highlighted a seasonality in the wind strength in the North Sea; the summer period has on average lower wind speeds than the winter period. Gerkema and Duran-Matute (2017) observed a similar seasonality in the wind climate in data from a weather station in the Dutch Wadden Sea, especially for southerly, southwesterly and westerly winds. They also found a high inter-annual variability for these directions. Northwesterly winds are rarer but can be strong. Of particular importance for our study is the orientation of the wind direction with respect to the coastline, which is at six degrees to the north, and hence northerly winds will favor a southward transport, and southerly and southwesterly winds a northward transport.

2.3. Wind and wave conditions during observation period

We analyzed how representative the two-year long record is compared to wind conditions over a 10-year period, by comparing the relative occurrence of strong and extreme wind conditions (defined as larger than 10 m/s and larger than 15 m/s, respectively) and the summed wind energy per sectorial direction, following (Gerkema and Duran-Matute, 2017). Overall, it turns out that the 2011–2012 time series is fairly representative for the wind conditions during the 10-year period to which we extrapolate the results.

For further analysis, the dataset will be split into calm and energetic conditions, for which the wave height or the wind speed can be used. The wave height was calculated from data from the bottom lander in van der Hout et al. (2017). At our study site a high correlation exists between both parameters (R = 0.81, Fig. 3), and hence energetic conditions reflect (most of the time) the joint effect of wave and wind energy. A wave height of 0.8 m marked the onset of elevated SPM levels resulting from bed shear stresses by wave energy (van der Hout et al., 2017). This corresponds to a wind speed of 5 m/s, which lies within the 3 Bft wind bandwidth. We will adopt either of these thresholds, depending on the context.

2.4. Dataset from bottom frame

The analysis is performed on a long-term, in-situ dataset from a bottom frame at the position indicated in Fig. 1; its location was 1.2 km offshore, at an average water depth of 11 meter. The frame was deployed at this location from February 25, 2011 until November 24, 2012, as part of the research project ‘Monitoring and Evaluation Program Sand mining’ commissioned by the La Mer Foundation (Witbaard et al., 2015, 2017). Due to failure of the ADCP only two consecutive periods are used in this study: April 8, 2011 until October 14, 2011 and January 10, 2012 until July 26, 2012. This amounts to almost one year of data, but this covers mostly summer months. Time series of several key variables were already shown in Figs. 4 & 5 in van der Hout et al. (2017).

The data used for the present analysis are the current velocities and wave height from an ADV at 0.15 meter above the bed (mab) and the calibrated SPM concentrations from four JFE-ALEC Advantech Compact-CLW’s (model ACLW-USB) OBS’s at 0.3, 0.8, 1.4 and 2.0 mab (Fig. 4). The OBS sensors were calibrated in the laboratory using sediment samples collected in the field from the same study site; for more details, see van der Hout et al. (2017). The sensor at 0.3 mab was the INFINITY version to measure turbidities > 2 gl^{-1}.

In addition, an upward-looking ADCP (RDI Workhorse Rio Grande 1200 MHz) was mounted at the top of the bottom frame. The 10-minute average of 30 pings was stored internally, the cell size is 0.25 m, with the first bin at 0.62 m from the transducer, which is at 2.62 meter above bottom (mab). An estimate of the SPM concentrations in the upper part of the water column is obtained by converting the acoustic backscatter (AB) of the ADCP to SPM concentrations, as described in Section 3.1.

A sketch of the bottom lander (Fig. 4, left panel) indicates the part of the water column monitored with the sensors at the bottom frame. All sensors were set to record with an interval of 10 min.

2.5. Dataset from anchored stations

For calibration and validation of the acoustic backscatter conversion of the frame-mounted ADCP, on two days anchored station (AS) measurements near the bottom frame were performed with RV Navicula. SPM concentration profiles over the entire water depth were taken with a Seabird CTD plus attached Seapoint OBS, following the protocol and calibration procedure as described in van der Hout et al. (2015). See Fig. 4 for a sketch of the data overlap of the AS dataset and the bottom

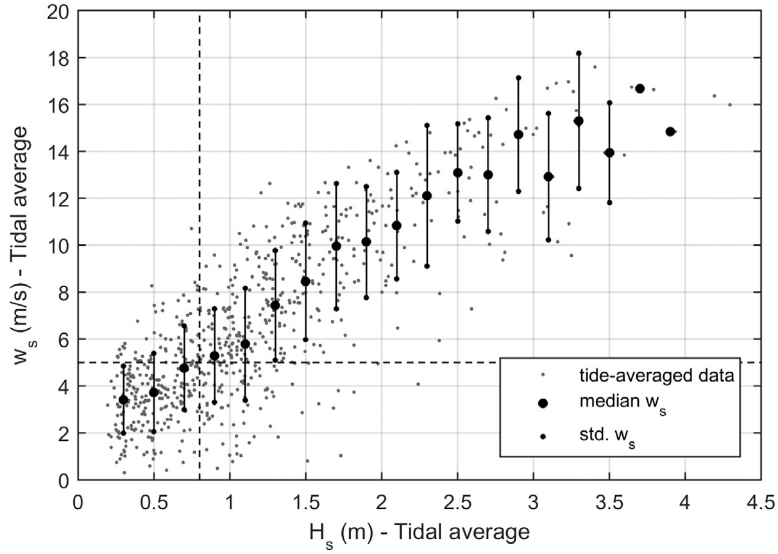

Fig. 3. Correlation between tide-averaged (zero-crossing) wind speed (w_s) and wave height (H_s). The correlation coefficient R of the data is 0.81. The median and standard deviation of w_s per subsample of H_s are shown with the large and medium black dots connected by vertical lines. The bin size is 0.2 m and n > 20. The dashed vertical and horizontal lines are drawn at $H_s = 0.8$ m and $w_s = 5$ m/s. These lines highlight the two thresholds applied in this chapter to separate the dataset in calm conditions and energetic conditions.

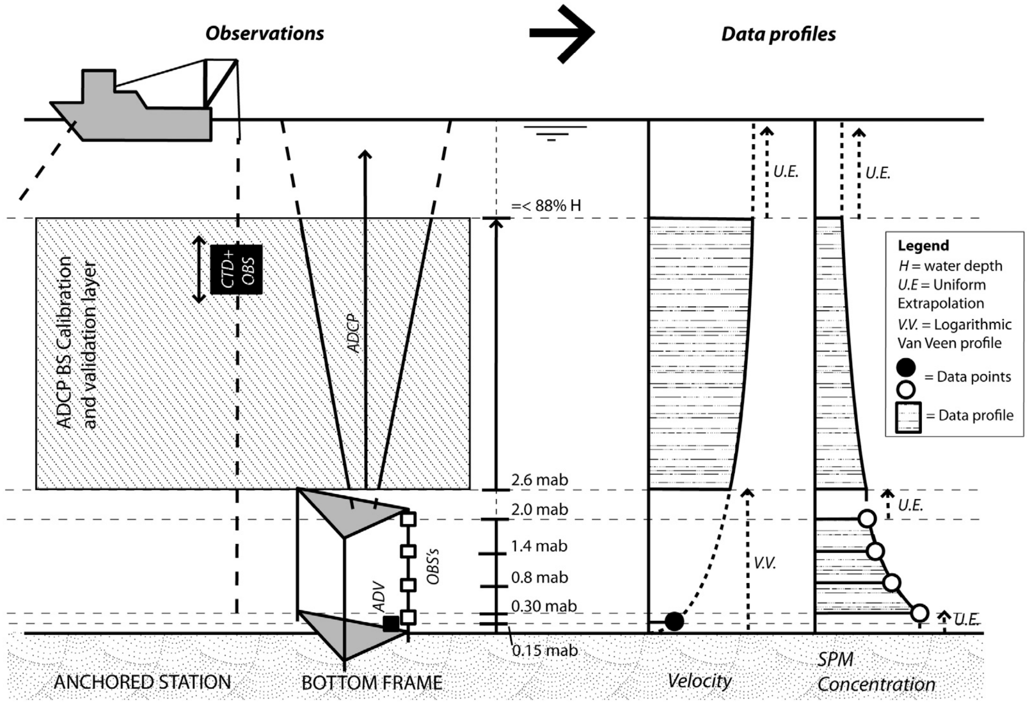

Fig. 4. Sketches of the observation methods (left-hand side) and the construction of the data profiles from the observations on the bottom frame (right-hand side). The overlapping area between the ship's CTD and the bottom frame's ADCP is highlighted as the hatched box titled the 'ADCP BS calibration and validation layer'. The instruments mounted onto the bottom frame that are used in this study are the upward looking ADCP, four OBS's (white squares) attached at 0.3, 0.8, 1.4 and 2.0 meter above the bed (mab) and an ADV at 0.15 mab (black square).

frame dataset. The AS dataset comprises 22 profiles on April 28, 2011 (AS2011) and 39 profiles on March 20, 2012 (AS2012). Profiles were taken every 20 min; the datasets encompass 7 h 20 min (AS2011) and 13 h (AS2012). The cross-shore distances between the ship location and the bottom frame were 235 m for AS2011 and 128 m for AS2012. Both datasets were obtained during calm conditions (significant wave height less than 1 m), when mostly fine-grained material is in suspension. This induces a bias for fine-grained suspensions of the calibration and validation dataset.

3. Calculation of SPM transports

This section describes the methods used to obtain SPM concentration and current profiles, used to calculate the SPM transports. This involves four steps. First, we explain how the acoustic backscatter (AB) of the ADCP is converted to SPM concentrations. Second, we outline the calibration procedure involving data from the OBS sensor at the top of the bottom frame as well as the ship-based SPM profiles derived from the CTD casts. Third, the profiles of current velocity and

SPM concentration are constructed by inter- and extrapolation, both spatially and temporally. Finally, the transport is calculated on a sigma-grid to facilitate the calculation of time-integrated values (as water levels vary over time).

3.1. Conversion of acoustic backscatter into SPM

The basic formulation for the conversion of the acoustic backscatter (AB) signal to suspended sediment concentrations is the sonar equation, which features a linear relation between the amount of back-scattered intensity and the amount of particles on which the sound is scattered (Urick, 1983; Deines, 1999). The AB-conversion is less commonly applied to cohesive sediment than to coarser grained sediment, as the scattering principle for coagulated sediments differs from the one developed for sand grains. Modified formulations for these situations have been developed by Hoitink and Hoekstra (2005) and Merckelbach (2006), and a more recent proposed adjustment by Thorne and Hurther (2014) is promising. However, these adjustments require the measurement over time of particle and floc sizes, which is unfortunately not available in our dataset.

Therefore, we apply the sonar equation, and add a correction of the count-to-decibel conversion as proposed by Gostiaux and van Haren (2010). Additionally, we add the near-field correction (ψ) for distances closer than the transducer near-field r_n (Downing et al., 1995), which is two meter from the sensor head for the ADCP in this study. The AB conversion equation applied in this study then reads:

$$10\log_{10}\left(10^{k_c E/10} - 10^{k_c E_n/10}\right) = A - 20\log_{10}(\psi R) - 2(\alpha_w + \alpha_s)R - 10\log_{10}(T_t + 273) + 10\log_{10}(C_{SPM}). \quad (1)$$

The parameters, in the order of appearance in the equation, are: k_c is the (beam-dependent) scale factor to convert counts to decibels (dB/count), E is echo intensity recorded per beam (counts), E_n is the noise level of the transducer taken as 46 counts (Gostiaux and van Haren, 2010), A is an instrument-dependent calibration parameter (in dB) that depends also on the type of suspension (Jourdin et al., 2014), ψ is the dimensionless near-field correction (Downing et al., 1995), R is the (slanted) distance from the transducer to the correct distance in the observed cell at one-fourth of the cell (m), as used by Gostiaux and van Haren (2010), α_w is the dimensionless sound absorption coefficient by water (Francois and Garrison, 1982), α_s is the dimensionless sound absorption coefficient by sediment, determined for each cell with 0.045 times the mass in suspension for a median particle radius of 10 μm (Urick, 1983; Hoitink and Hoekstra, 2005), T_t is the transducer temperature (°C) and C_{SPM} is the SPM concentration (kg/m^3). The temperature correction accounts for the 2–20 °C temperature variation over a year, whose variation has a stronger effect on the correction for the absorption coefficient by water (α_w) than on the correction for the instrument temperature (fourth term on the right-hand side of the equation). Measured SPM concentrations at two meter above the bed regularly exceed 100 mg/l (van der Hout et al., 2017), thus the attenuation by sediment (α_s) at the transducer head is significant at times (Jourdin et al., 2014).

3.2. Calibration procedure

Eq. (1) requires the calibration of two parameters; k_c and A, being beam- and location dependent, respectively. The acoustic calibration also depends on the grain size distribution of the suspension, thus in-situ calibration is essential (Hoitink and Hoekstra, 2005). Both parameters are commonly calibrated with simultaneously operating OBS sensors. In this study, a standard calibration of k_c and A with the ship-based AS datasets proved unsuccessful, as the calibration with the AS2011 subset gave a weak correlation for the validation with the AS2012 subset. This result is likely due to differences in sediment composition, floc composition or phytoplankton communities between both subsets. Therefore, another approach is adopted here; k_c is calibrated by aligning the slope of the concentration profile of the moored ADCP with the slope of the concentration profile from the ship-based AS2011 subset, and A is calibrated per time step with the SPM concentration measured at the top of the bottom frame by the OBS. This approach offers a satisfactory validation with the ship-based AS2012 dataset, as described below. In this calibration process, the SPM concentration is uniformly extrapolated from 2.0 to 2.6 mab (Fig. 3), which introduces a relatively small error with respect to the uncertainty surrounding the ADCP-based observations. The calibrated values of k_c (Table 1) are relatively low compared to other studies, which are generally near 0.45 (Sahin et al., 2017). The calibrated values of A vary not only between the beams but also over time. The temporal variation has among other scales a tidal signal, which may be a compensation for the missing term for the backscatter variation due to floc size variations over time in Eq. (1). Parameter A also shows a slow increase over time, which is related to the echo emission decrease over time of the ADCP transducers. The difference in α_w within and between the studies comes from the difference in water temperature and salinity.

Table 1
Parameters in the AB conversion equation (Eq. (1)) for a 1.2 MHz ADCP (k_c and A); their range of values as determined in this study and in literature. The range applies to the four beams (k_c, A), to the variation over the vertical (α_w) and over time (α_w, A). The values for α_w are determined with the equation by Francois and Garrison (1982), and depend on water salinity and water temperature.

Parameter	Value	Study
k_c (dB)	0.35–0.55	Deines (1999)
	0.43	Kim and Voulgaris (2003)
	0.40–0.44	Sassi et al. (2012)
	0.36–0.37	This study
A (dB)	129	Deines (1999)
	105	Kim and Voulgaris (2003)
	83–90	Sassi et al. (2012)
	75–90	This study
α_w	0.48	Kim and Voulgaris (2003)
	0.25–0.29	Sassi et al. (2012)
	0.43–0.67	This study

3.3. Validation

Validation of the SPM concentration profiles is done with the AS2012. The overlapping vertical distance of the calibration and validation layer is marked in Fig. 4. AS2012 is a challenging dataset for validation purposes as strong vertical and horizontal gradients in the SPM concentrations near the seabed were present, with differences in concentrations up to 100 mg/l in both directions. The large horizontal differences in SPM concentrations between the bottom frame and the AS are due to the cross-shore distance between the two observation methods within this high turbidity zone, which is 128 m for this dataset. The validation dataset shows a variation in the vertical concentration profiles that ranges from sharp SPM stratification at pycnoclines (observed in six out of 39 profiles) to uniform low concentration profiles. The transition from stratified to uniform, and vice versa, appears to have a slight phase difference between the ship and the bottom frame observations of approximately 30 min, despite the small distance between the two. The two profiles that experience this state difference are distinctly marked in Fig. 5B, where profile 4 is the profile change from stratified (bottom frame) to uniform (anchored station), and vice versa for profile 38. In other profiles, the vertical position of the SPM stratification is remarkably well reproduced by the ADCP. The correlation between the ship-based SPM concentrations and the bottom frame SPM concentrations for 2012 is significant ($R^2 = 0.62$, Fig. 5B). The correlation of AS2011 is slightly lower, but also significant ($R^2 = 0.54$; Fig. 5A).

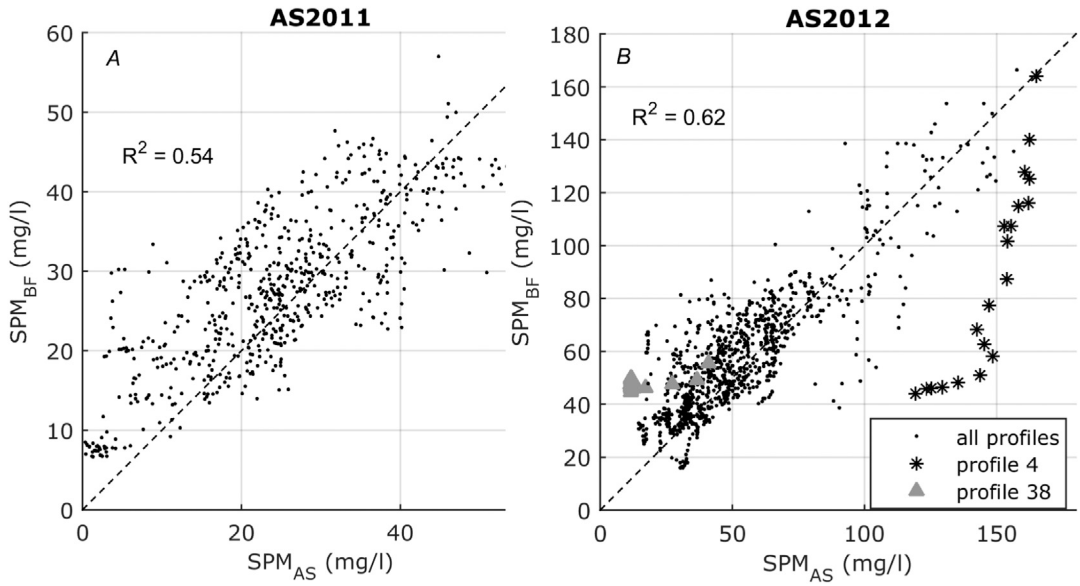

Fig. 5. Correlations between the SPM concentrations of the bottom frame (SPM_{BF}; y-axis) and the ship-based, anchor station SPM concentrations (SPM_{AS}; x-axis) of the calibration (panel A: AS2011) and validation (panel B: AS2012) datasets. Note the difference in axis scaling between the two datasets. The correlation coefficient is noted in the top left corner of the graphs. In panel B two vertical profiles (profiles 4 and 38) are highlighted with different markers that form outliers due to a difference in SPM stratification between the two locations, see text.

3.4. Velocity and concentration profiles

The data to construct the velocity profile from the seabed up to the water surface are the ADV data at 0.15 mab and the ADCP data ranging from 2.62 mab up to 88% of the water depth (Fig. 4). The depth of the top layer of the ADCP data is determined from the quality of the acoustic signal, which reduces greatly under storm conditions due to wave-induced bubble entrainment in the surface layer. The near-bed profile between the ADV and the first observation of the ADCP range is interpolated with a power-law profile; $u = aH^{1/5.2}$ (van Veen, 1937), where H is the height above the bottom and a is a constant calibrated by fitting the velocity profile to the data in the lowest 4 meter of the water. We applied a uniform extrapolation from the top of the ADCP profile up to the surface. Near-surface effects from wind drag are thereby neglected.

The near-bed SPM concentration profile is constructed from linear interpolation between the data at 0.3 mab, 0.8 mab, 1.4 mab and 2.0 mab from the OBS observations attached to the bottom frame. From the seabed to 0.3 mab the concentration profile is taken uniform. The upper part of the profile is inferred from the ADCP AB-conversion at 0.25 m intervals. We applied a uniform extrapolation up to the surface.

3.5. Transport calculation

Both the velocity profile $u(z)$ (of the alongshore current) and the concentration profile $C(z)$ are interpolated onto the same z-grid to calculate the transport ($q(z) = u(z) \times C(z)$), which is then transformed to σ-layers (i.e., layers of adjustable thickness) to accommodate the free-surface movement; we use 41 $\sigma-$ layers.

For most purposes we calculate depth-integrated transports either over the ebb or flood phase (gross transport), or over the full tidal cycle (net transport). Tidal cycles with large time gaps (during frame service days and sometimes storms) are left out of the analysis. The tidal cycle is determined as the period between two downward zero-crossings of the current (i.e. the period between two successive flood-to-ebb slacks), to account for variations in the length of the tidal period due to tidal harmonics and atmospheric variations.

Besides the depth-integrated transport, we determine the mean (q_{mean}), and the root-mean-square (q_{rms}) of the fluctuations $q\prime$ from the quickly varying transport q per layer over the M_2-tidal period, with:

$$q\prime = q - q_{mean} \tag{2}$$

, following the methodology of Becherer et al. (2016). Fig. 7C shows this exercise. The value and sign of q_{mean} indicates the magnitude and direction of the residual transport for layer 5 while q_{rms} is always a positive value and marks whether the residual transport is a result from equaling relatively large or small northward and southward transports.

4. Results: Gross transports

The ebb and flood gross mass transports (GMT) are calculated as the tidal-phase integrated and depth-integrated transports. These quantities are an indication of the total volume of SPM that is moved back and forth with the tidal current. In contrast, the net transport reflects the (im)balance between the transports of the two tidal phases.

4.1. Calm versus energetic conditions

Here, the split into calm and energetic conditions is based on the wave height threshold of 0.8 m (Fig. 3), but it makes sense on basis of the wind characteristics as well. The weak winds are characterized by a homogeneous distribution over all directions (Fig. 2), which prevents a bias towards a prevailing wind direction. Wave heights above the threshold generally correspond to stronger winds, which may affect the current and introduce preferential directions.

In Fig. 6 scatter plots and distribution graphs are shown for the GMT in the ebb (horizontal) and flood (vertical) phases GMTs; on the left, for calm conditions, on the right, for energetic conditions. The normalized histograms indicate that GMTs are mostly in the order of 0 – 6 ton/m per tidal period. Large GMTs (> 6 ton/m) are found mainly in the flood phase during energetic conditions.

Both scatter plots indicate that the flood GMT is generally larger than the ebb GMT of the same tidal cycle, as the majority of the scatter points is situated above the diagonal line (indicating equal transport masses). The data of the energetic conditions are more widely scattered

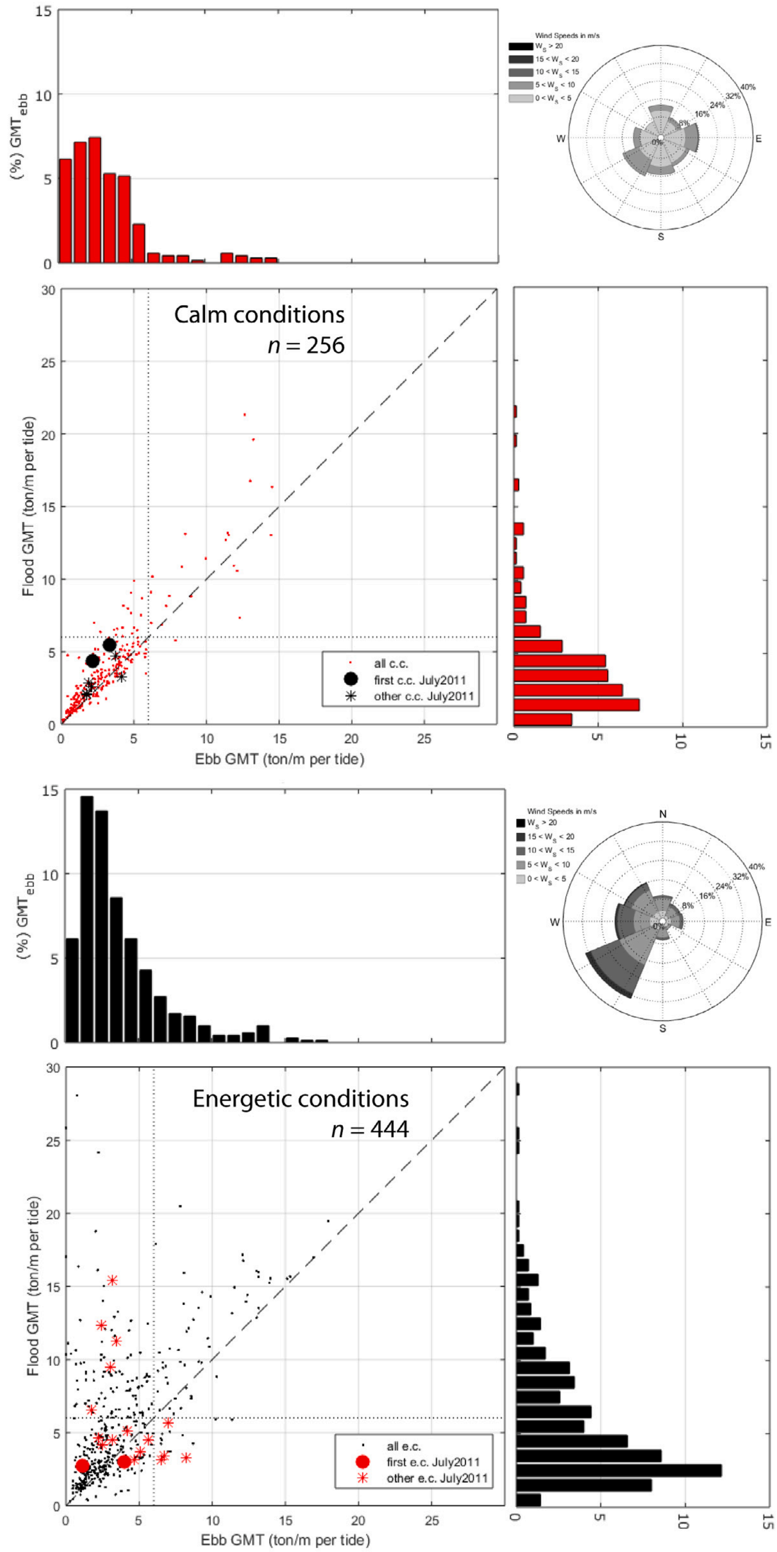

Fig. 6. Gross mass transport (GMT) per type of conditions, top panels (in red) for the calm conditions and lower panels (in black) for the energetic conditions. The scatter diagrams show the flood GMT versus the ebb GMT. The diagonal black dashed line in the scatter plot shows the line of equal transport mass. The horizontal and vertical dashed lines mark the GMT transport of 6 ton/m. The triangles and stars mark the tides from the time-series shown in Fig. 7. The normalized histograms at the sides of the scatter diagrams show the percentages of the ebb and flood GMT in the dataset. The bin size is 1 ton/m. The percentage of GMT is calculated as the number of tides per bin divided by the total number of tides in the dataset (which is 700). Thus the GMT_{ebb} of the calm and energetic conditions add up to 100%, as with the GMT_{flood}. In the upper right corners of each set of panels is the wind rose of the conditions given.

and farther from the diagonal. This indicates that the difference in gross transports between the ebb and flood phase is larger, which implies a larger net mass transport (NMT) during these energetic conditions. In contrast, the calm conditions scatter is more aligned with the diagonal line; hence, the net mass transport (NMT) will be relatively small. Thus, the difference between calm and energetic conditions is more

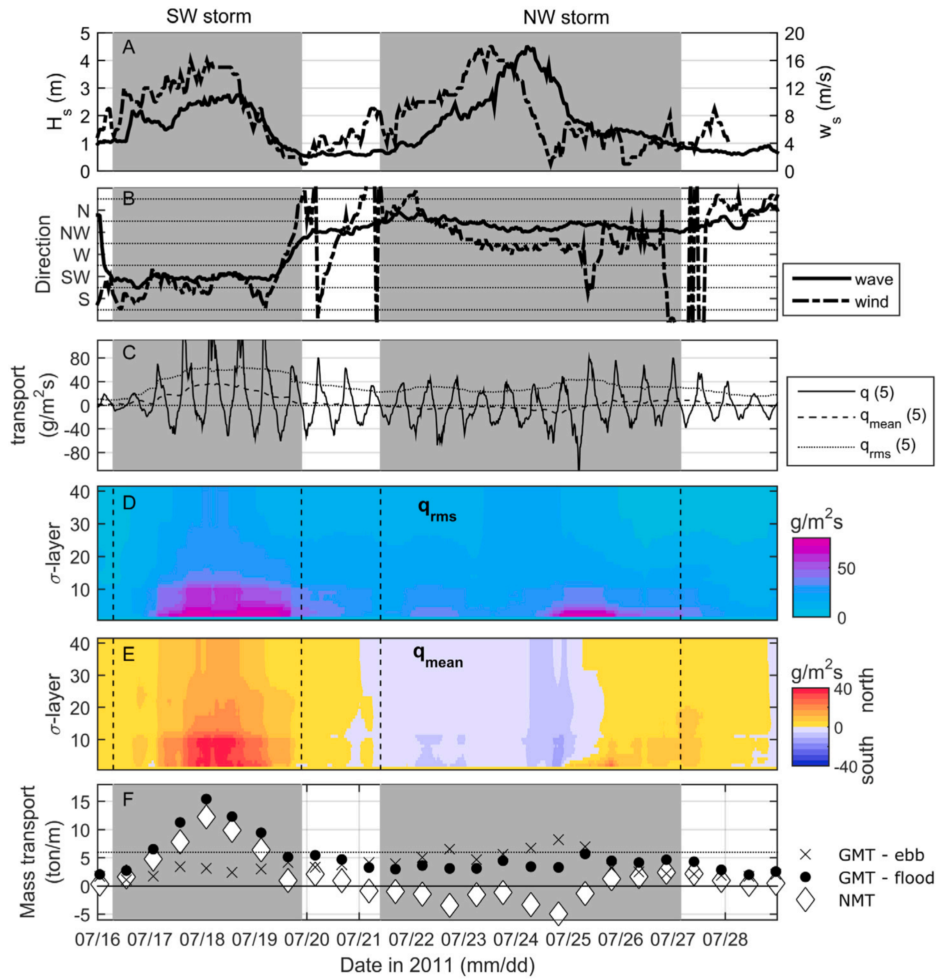

Fig. 7. Time-series of two storms from opposing directions; SW and NW storm, both storm periods are indicated by the gray boxes (A, B, F) and vertical dashed lines (C, D). It is quite unique that the storms are intermittently separated by more than a day of calm conditions (white boxes). Panel A: wave height (H_s) and wind speed (w_s). Panel B: wave and wind directions. Panel C: transports at one layer ($\sigma = 5$); raw transport (q), and the derivations of the gross and residual transport parameters, q_{rms} and q_{mean}, respectively. Panel D: depth-variation of the gross transport q_{rms}. Panel E: depth-variation of the residual transport q_{mean}. Panel F: the flood and ebb GMT (Gross Mean Transport) and the NMT (Net Mean Transport) of the considered storm period.

pronounced in the net than in the gross transports. The question of why the difference is not very marked in the gross transports, will be addressed in the following subsection.

4.2. Details of a storm period

We have selected a unique sequence of a SW storm directly followed by a NW storm to analyze the temporal variation in a storm period, shown in Fig. 7. The uniqueness lies in the fact that calm conditions precede, separate and succeed these two storms and that the wind and wave directions are relatively constant during both storms. The maximum wind speed during each of the two storms was about 17 m/s, but the maximum wave height differed and was 2.8 m and 4.5 m during the SW and the NW storms, respectively (Fig. 7A). Their duration was 3.5 days (SW) and 6 days (NW), which is highlighted in the panels by the gray areas.

The variation in q_{rms} (a measure of the fluctuation in the transport) over the two storms resembles largely the variation in the wave height, be it with a delay between half a day and a day (Fig. 7D). In the calm period between the two storms q_{rms} decreases a little, but a return to the initial calm levels occurs only in the aftermath of the second storm. During the NW storm the q_{rms} in the surface layer also follows the wave height with a delay of about half a day, but q_{rms} in the bottom layer only increases to the peak value when the wave height starts to decrease on July 25. These observed lags of the response of q_{rms} to H_s become even more apparent from the hysteresis that appears when plotting these parameters against each other (Fig. 8). The curve of the depth-averaged q_{rms} contains a weaker hysteresis than that of the near-bed layer. This is because not all layers respond similarly as the bottom layer to a variation in H_s due to the delayed process of upward resuspension and settling of SPM (Yu et al., 2011). The occurrence of a hysteresis shows that, for a certain wave height, the near-bed q_{rms} can have multiple values depending on whether the storm is developing or decaying. The lag of the response in the near-bed layer in this figure appears to be half a day for increasing conditions (the order of a tidal cycle) and more than a day for decreasing conditions (the order of two tidal cycles).

This hysteresis implies that different gross transports may occur for similar wave heights. This offers an explanation of why the strength of the gross transports does not very distinctly follow the separation in calm and energetic conditions (Fig. 6). This is illustrated in the scatter plots of Fig. 6, where the data points of the selected storm period are marked with an asterisk and the first two data points after a change of conditions with large dots, which are referred to as lag markers. As expected, the lag markers show up as outliers in both scatter plots: in the graph of the calm conditions the lag markers are located furthest from the origin and in the graph of the energetic conditions the lag markers are located closest to the origin. Thus, the lagged response of the gross transports to a change in conditions is a cause for the spread in the scatter plots. Additional factors (not investigated here) may lie

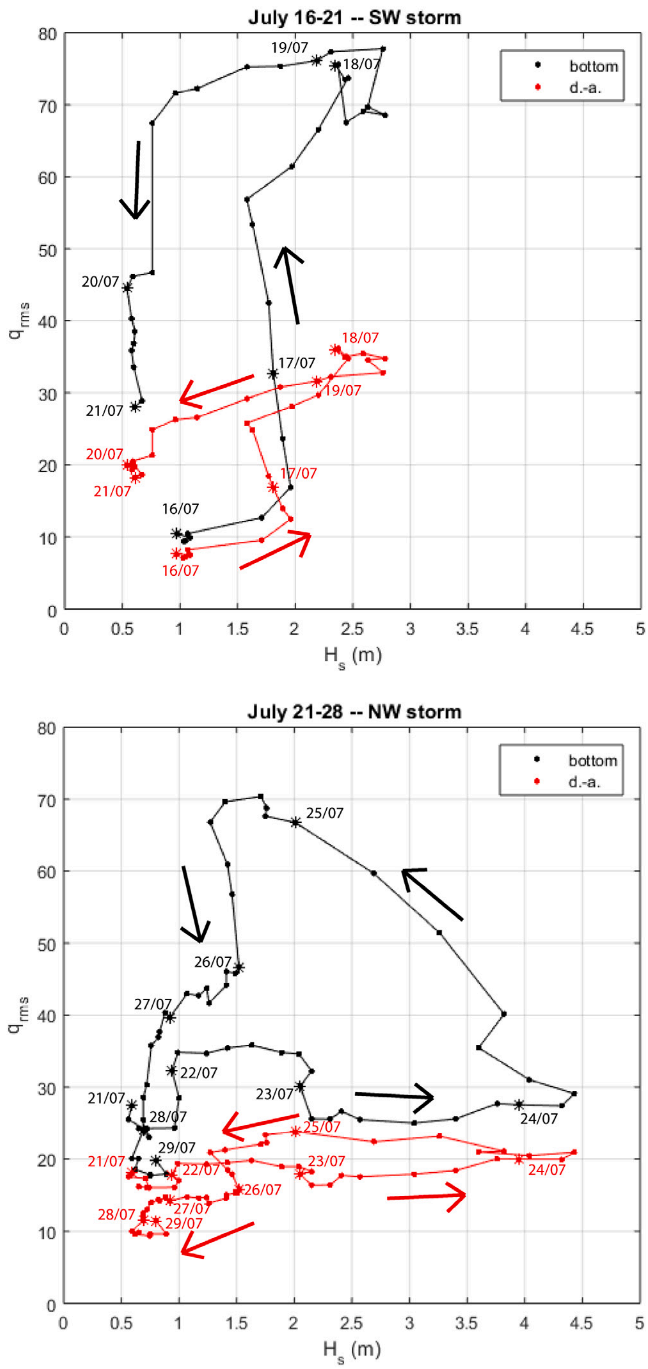

Fig. 8. Sequential scatter plots of the gross transport amplitude (q_{rms}) versus the wave height (H_s) for the time-series of two storms; SW storm (left) and NW storm (right). The time between dots is 3 h, and the first datapoint of a day is annotated with the date. The bottom data are from the third σ-layer above the seabed which is a distance of approximately 0.8 mab (bottom; black line) and the red line shows the depth-averaged value of q_{rms}.

in the non-local character of the signal, notably the role of cross-shore displacement of the TMZ with respect to the fixed bottom frame.

5. Results: Net transports per tidal cycle

5.1. Storm sequence and wind direction

The net transport results from the imbalance between the gross transports of the tidal phases. Its value q_{mean} – defined as the running mean over one tidal period (Eq. (2))– is shown in Fig. 7C and E for the July 2011 storm episode. Panels D and E show that the largest net transports occur near the seabed and during the storms, as was observed for the gross transports. During the calm conditions the direction of the net transport is generally northward but with a small magnitude (<5 g/m^2 s). During the SW storm the net transport is northward, and turns southward during the NW storm, as one would expect for these winds along a coastal boundary. In the storm sequence in July 2011 two highlights are found that demonstrate the influence of the wind direction over the wave direction on the net transport direction. The first is the change of the net transport to southward before the NW storm commenced (indicated by H_s = 0.8 m). This was induced by an increase of the wind speed from below 5 m/s to 8 m/s during that same short period before the wave threshold was reached (Fig. 7A). The wind and wave directions had already changed from SW to NW at the start of the intermittent calm period, but the direction of the net transport only changed for larger wind speeds. The second highlight shows in the aftermath of the NW storm (on July 25th). The net transport changes back to northward, while the wave conditions remained unchanged from the north. The only change was in a relaxation of the wind speed.

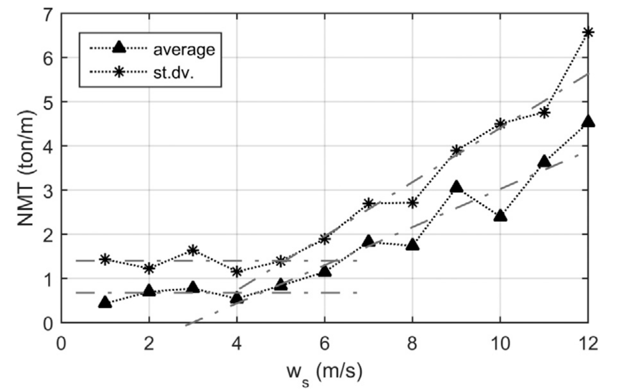

Fig. 9. The mean and standard deviation (st.dv.) of the NMT per wind speed bin of 1 m/s. Trend lines are drawn with the gray dash-dotted lines through the data points of the mean and standard deviation. The horizontal and sloping trend lines intersect roughly at w_s = 5 m/s.

In this section we will divide the data again in calm and energetic conditions. Here we base this on the wind speed, as the details in the storm sequence hinted towards. In Fig. 9 we show the average NMT and its standard deviation per 1 m/s wind class. Both parameters appear to follow a similar trend: for low wind speeds they have a constant value, but at higher wind speeds they increase linearly with wind speed. The horizontal and sloping trend lines cross roughly at w_s = 5 m/s, shown by the dashed lines. This observation leads us to regard w_s = 5 m/s as the threshold which marks the onset of wind effects on the net transport, which substantiates our definition of calm and energetic conditions.

5.2. Calm conditions

Fig. 10 gives a broader overview of the influence of the direction and magnitude of the wind on the net mass transport per tidal cycle (NMT) by showing all data in the dataset. The black dots in Fig. 10 mark the NMT at low wind speed conditions, and they are aligned near and around zero, except for a few outliers. The scatter for low wind speeds in Fig. 10 suggests that the wind direction does not play a role during the calm, almost windless conditions, as the NMT varies more or less in the range from −2 to + 5 ton/m regardless of the wind direction. Distributions of probability density functions (not shown) confirm this: for all eight wind sectors, the NMT for periods with w_s < 5 m/s approach a normal distribution with a mean and median in the range

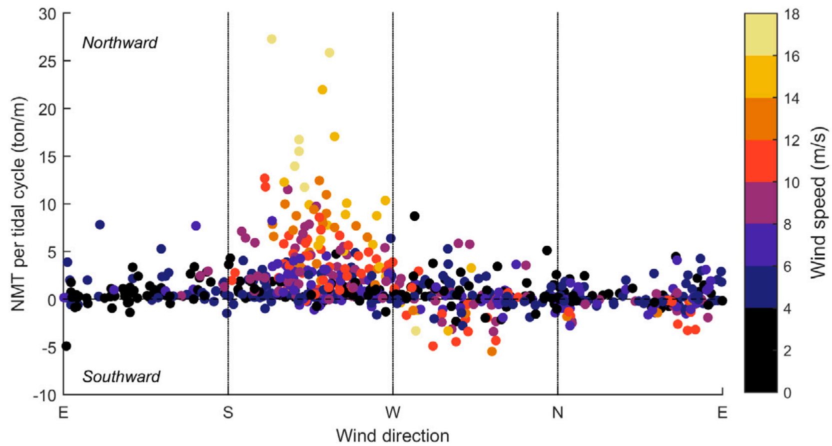

Fig. 10. The net mass transport per tidal cycle (NMT) shown against the wind direction per tidal cycle, with colors indicating the mean wind speed.

between 0 and 1 ton/m, and hence no significant effect of the wind direction is detected. A slight skewness indicates that occasional larger northward NMTs occur more often than southward ones.

These conditions therefore give the tidal and density driven effect on the transport of SPM. We can estimate the typical net transport during these calm conditions from the median of the subset, which is 0.4 ton/m. The standard deviation is 1.6 ton/m, which illustrates the high variability of the NMT during these conditions, which originates from various factors, such as the aforementioned delayed response in the GMT.

5.3. Energetic conditions

Clearly, the largest northward NMT occurs for strong South-to-West wind directions and the largest southward NMT occurs for strong North-to-West directions (Fig. 10). This pattern matches more or less the shoreline orientation, which is almost North–South at the study area. With a local coastline orientation of six degrees east of north, the flood (ebb) current is enhanced during a SW (NW) storm and the ebb (flood) current is decreased. The effect of the wind direction on the gross and net transports can be seen in Fig. 7C: during the SW storm the ebb GMT is smaller than during the calm period, while the flood GMT is larger. This leads to large northward values of the NMT in the same order of magnitude as the flood GMT. The opposite occurs for the NW storm. The GMT values in this figure show however that the amount by which GMTs are enhanced or decreased is not equal for the two wind directions. This points to an asymmetry in the net transport for SW and NW wind directions.

The effect of the wind direction on the transport direction is further explored in Fig. 11 (middle), which gives an interpolated visualization of the mean NMT per wind sector. The low wind speed data that mark the weak northward NMT during calm conditions stand out as the yellow blob around the center. The uniformity in tone in the yellow-colored region confirms the independence of the net northward transport on wind direction during calm conditions. The pattern of the mean southward (blue) and the mean northward (orange and red) net transport confirms the north–south relation between the direction of the net transport and the wind direction, as already observed in the July-2011 storm episode and in Fig. 10. The sharp division between the northward and southward transport is marked with a solid black line. Remarkably, this line is not exactly perpendicular to the coastline – which is at six degrees to the north at the study area – but rather oriented perpendicularly to the central axis of the Southern Bight, as shown by the dashed black line in Fig. 11, left. The angle of the central line of the Southern Bight (dashed line) is approximately 25 degrees to the north. This suggests that the geometry of the Southern Bight may affect the magnitude of the net transport for the various wind directions.

Table 2
Parameters for the statistical fit of the five cases. The statistical models are: the linear regression (Eq. (3)) and the normal distribution (Eq. (4)). The *p*-value for the linear regression of cases 1-4 is <0.05.

Case	Wind dir.	Wind dir. (deg)	w_s (m/s)	Size subset	a	b	μ	Eq.	σ
1	S&W	155°–185° 245°–280°	>5	73	0.33	−0.88	–	(3)	2.11
2	SW	185°–245°	>5	171	1.09	−6.10	–	(3)	3.23
3	WNW-E	275°–85°	>5	168	−0.21	1.55	–	(3)	1.66
4	SE	85°–155°	>5	16	–	–	1.36	(4)	1.42
5	All	All	<5	253	–	–	0.42	(4)	1.42

In any case, it is evident that above the wind-speed threshold of 5 m/s a relation exists between the magnitude of the NMT and the magnitude of the wind speed, as the colors intensify towards the edges of the NMT wind rose (Fig. 11, middle). However, the relation between the two parameters varies per wind direction as the maximum mean northward NMT are larger than 5 ton/m per tide while the maximum mean southward NMT barely reaches 3 ton/m per tide. This difference is too large to be ascribed to the tidal net transport, which was previously estimated to be 0.4 ton/m per tide in northward direction.

5.4. Regression per wind direction

To derive a relation between the wind direction, wind speed and NMT, the last one is shown against wind speed (only for data with $w_s >$ 5 m/s) per 10 degree-wind direction class amounting to 36 relations. To arrive at a workable number of regressions for further analysis, we have clustered them (according to their similarity) into the four sectors shown in Fig. 11, right panel. They are named after their dominant directions (N, NE, E, etc.). The linear regression for the wind sectors S&W, SW and WNW-E yields significant regressions, while no relation is observed for the SE sector (Table 2).

6. Empirical model for residual transport based on wind data

One of the goals of this paper is to estimate the long-term net transport of SPM in the TMZ. For this the length of the present dataset unfortunately falls short, as winter months are missing due to failure of the ADCP. The SPM transport dataset has a length two times six months (i.e. from April 2011 till mid-October 2011 and from mid-January 2012 till July 2012). Fortunately, the analysis of the gross and net transports in the previous sections has led us to the understanding that one can, in a statistical sense, estimate the net transport at our

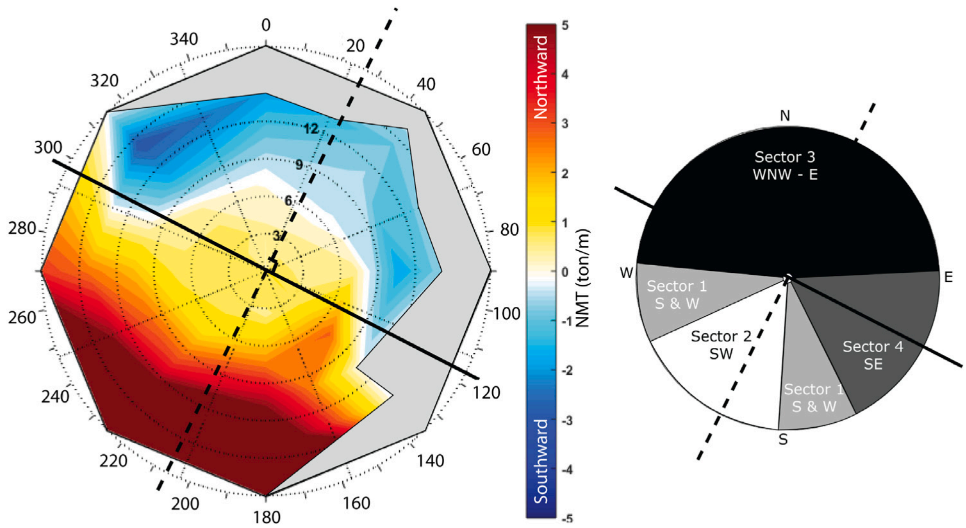

Fig. 11. Wind directions and geometry of the Southern Bight. Left: NMT wind rose of the net transport per tide (NMT) of the dataset, obtained by taking the mean NMT per wind bin (bin sizes: Δw_s = 3 m/s and Δ(direction) = 45°). The gray area covers the wind bins with two or less observations in the dataset; these wind conditions do not occur (often). On top is an outline dividing the northward and southward transport, with an angle that matches 25 degrees to the north. Right: Wind diagram filled with the four wind direction sectors; South and West together (Sector 1), the Southwest (Sector 2), the West-Northwest up to the East (Sector 3) and the Southeast (Sector 4). On top is the outline from the left panel.

study site from the average wind direction and wind speed during a tidal period. Implicit in this wind-NMT relation is the contribution of the wave height to the gross and net transports. In this section we will use linear regression to build an empirical model in order to find an estimate of the (multi-)annual residual transport from historic wind data.

6.1. Regression model

For the empirical model, we consider five cases that require a separate equation between the NMT and the wind speed: the four wind sectors (Section 5.4) and the calm conditions case (Section 5.2). For three wind sectors a linear relation is established between the NMT and wind speed in Section 5.4: namely, for the sectors SW, S&W and WNW-E. For the SE case the mean value (μ) of the normal distribution will be adopted, as well as for the case of calm conditions. Hence, the equations for the five cases are:

$$\mathrm{NMT}(j) = a_k w_s(j) + b_k \qquad \text{for } k = 1,2,3 \tag{3}$$

$$\mathrm{NMT}(j) = \mu_k \qquad \text{for } k = 4,5\,, \tag{4}$$

where j is the index for the tidal cycle, k for the case number; w_s is in m/s and NMT is the net mass transport in ton/m in tidal cycle j. The linear regression parameters (a_k and b_k) and μ_k are listed in Table 2. The model is completed by summing the NMT of the tidal cycles over the period under consideration:

$$Q = \sum_{j=1}^{n} \mathrm{NMT}(j)\,, \tag{5}$$

where Q is the residual transport in ton/m over a period of n tidal cycles. We distinguish periods of a month (Q_m) and a year (Q_y).

The model estimate of the NMT and the data overlap reasonably well (Fig. 12). The model does not capture the magnitude of the extreme values, but this is to be expected from a regression analysis. More interestingly, the model underestimates the NMT in the period January 2012–March 2012. As the present dataset covers mostly the summer period (10 are summer months), and only October 2011 and Jan–March 2012 for the winter period, the regression model may not exactly represent the year-round transport. This observation could hint at a difference between transport processes in winter and summer. A difference in SPM transport between the winter and summer periods is not only to be expected from a difference in wind climate between these two half-years (Siegismund and Schrum, 2001; Gerkema and Duran-Matute, 2017), but also due to a difference in strength and composition of the flocs (Fettweis et al., 2014). The summer period is marked by a stronger activity by biota, which causes both a larger fall velocity of the flocs and an increase in the resuspension threshold at the seabed. In winter the smaller fall velocity and easy erodability leads to longer suspension periods of SPM, and hence larger gross and most likely larger net transport rates. From the model-data comparison (Fig. 12), it seems that this may lead to a stronger relation between the NMT and the wind speed in the winter period. This caveat should be kept in mind in the estimates to be made in the following section.

6.2. Extrapolation to monthly and annual transports

The mean wind direction and wind speed are calculated per M_2 tidal period by dividing the 10-year time-series from 2004 to 2013 of the IJmuiden weather station into equal periods of 12.4 h. The 10-year wind dataset is used as input for the model to calculate the residual transport per year, Q_y (Fig. 13, black line).

The contribution of case 5 (calm conditions) to the residual transport is 0.11 kton/m per year. Here, we expect tidal asymmetries to be the main driver, and a minor contribution of the density gradients. Of course, this tidal contribution acts not only during calm conditions but also during energetic ones. For the entire time period, this would then imply a residual transport of 0.3 kton/m per year in the northward direction, due to tides.

The mean annual residual transport for all conditions taken together (thus including the wind-driven component), is found to be 1.0 kton/m (horizontal dashed line or gray line, Fig. 13). For individual years, low and high extreme values of 0.6 and 1.3 kton/m occur in 2010 and 2008, respectively. These numbers are a factor of two apart, which highlights the variability of Q_y due to the annual wind climate. The inter-annual variability is of a similar order of magnitude as observed in the Dover Strait transports (van Alphen, 1990; de Kok, 2004; Fettweis et al., 2007). The SW case shows the highest annual wind energy. The wind rose for energetic conditions in Fig. 6 shows that SW winds occur two times more often than NW winds, which favors northward directed net transports. The SW case also has the strongest regression coefficient with the NMT in the model and thereby forms the dominant factor in the magnitude and the variation of the northward transport. Indeed, a

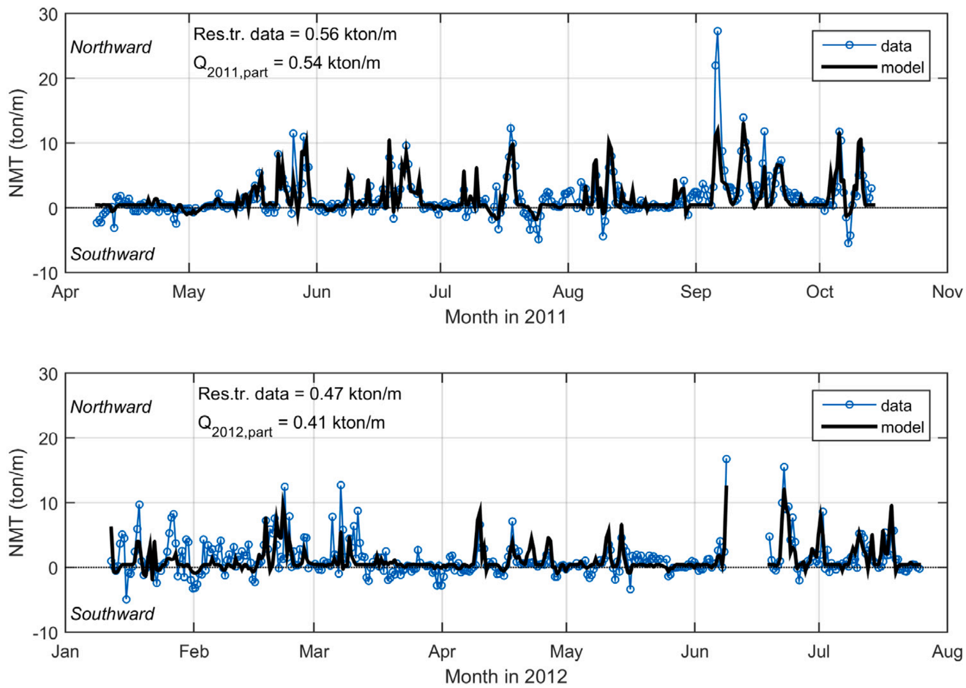

Fig. 12. Time-wise overlay of the modeled NMT (q) and the data NMT in 2011 (top panel) and in 2012 (bottom panel). The summed residual transports of the total period of the data (Res.tr. data) and of the model (Q_y) are shown in the top left corner of the graphs.

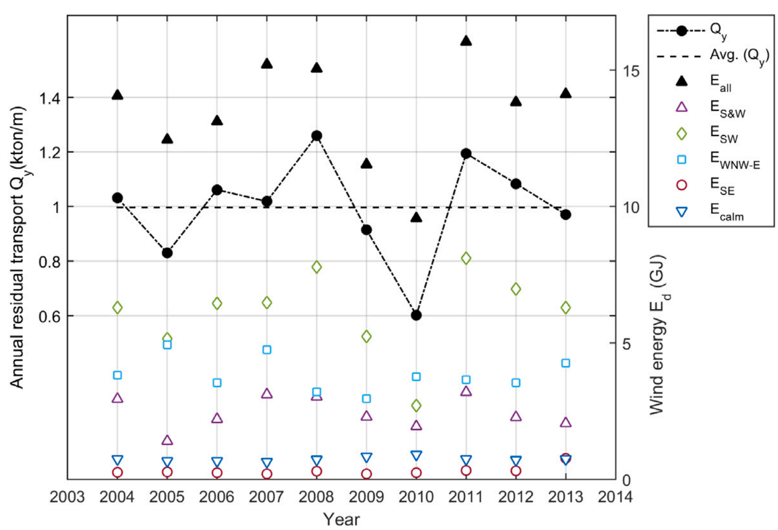

Fig. 13. The ten-year modeled variation of the (northward) annual residual transport (solid black circles and dash-dotted line) and its mean annual transport (dashed black line) shown along with the summed annual wind energy for all directions (E_{all}; black triangles), per model case (E_d and E_{calm}; colored markers).

clear similarity can be observed in the patterns of the residual transport and the wind energy of the SW case (comparison of the green diamond markers and the black solid line in Fig. 13). The cases WNW-E and S&W have respectively an opposing and amplifying effect on the residual northward transport, but the effect is minor. The year 2010 stands out as exceptional, with low total (and SW) wind energy levels. This was also seen in unusual export of water through the Marsdiep tidal inlet for that year in a modeling study by Duran-Matute and Gerkema (2015).

Fig. 14 shows the modeled averages of monthly transport values (Q_M), divided in a wind part and a tidal part. The wind part per month (Q_M-wind) is determined by subtracting an assumed constant value for the monthly tidal part (Q_M-tide; 0.4 ton/m per tidal cycle (Table 2) gives 0.024 – 0.025 kton/m per month depending on the number of days in a month) from the monthly mean. (Q_M)-wind shows a seasonal variation with lowest values in April and May, and highest values in December and January. The extremes are a factor five apart. The difference between the two seasons may be even larger than modeled here, as the model showed an underestimation for the two winter months January and February 2012 (Fig. 12). The underlying regression is steered towards summer months, due to the data availability. The variation in Q_M is mostly due to the variation in the wind energy of the S&W and the SW cases over the year. The wind energy of the WNW-E case does not vary much in this wind record. The bottom frame data show that in summer, the tidal part of Q_M can be equal to the wind-driven part and occasionally even higher. In winter, it is the reverse, the wind-driven part is higher than the tidal part.

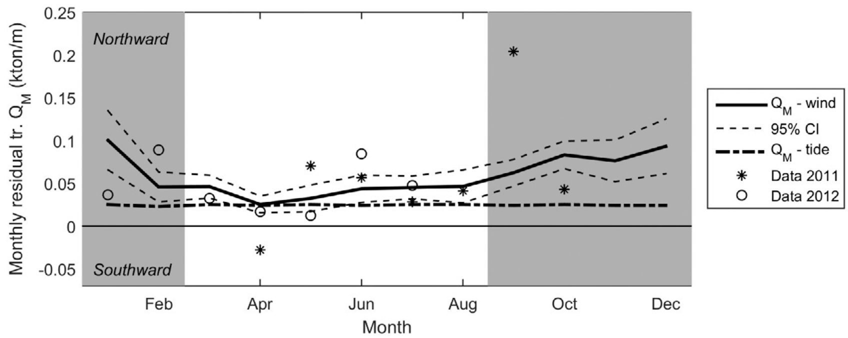

Fig. 14. The modeled monthly residual transport (Q_M) divided in the windy part (mean and 95% confidence interval) and the tidal part. The wind part of the data is shown with markers for the available months in 2011 (stars) and 2012 (circles), and calculated similar to the modeled data for reference purpose. The gray (white) areas mark the winter (summer) months.

7. Discussion

The estimate of 1.0 kton/yr of the residual longshore transport has been determined for a single position in the turbidity maximum zone (TMZ). Hence the transports come in kton/m, the latter standing for the distance in the cross-shore direction. More broadly, we aim to overcome this limitation and establish an estimate of the longshore transport in the TMZ by means of an extrapolation of the bottom frame data in the cross-shore direction. Multiple observations showed a fairly similar concentration distribution over the cross-shore area of 0.5 to 3 km from the shoreline (van der Hout et al., 2015). Even though the small zone between 0.5 and 1 km is rather steep as it is the upper shoreface, and will likely experience larger wave-driven currents during storm conditions, we will include this zone in the budget estimate as the area contributes largely. Extrapolating the average annual northward transport of 1.0 kton/m over the cross-shore distance of 2500 m gives an estimate of the transport in the TMZ of 2.5 Mton per year. Compared to the estimate of 22 Mton/yr from the literature mentioned in Section 1, this is rather low nor does it lie within the uncertainty bands of 8–32 Mton/yr. We should however note our estimate is most likely conservative as the model inhibits an underestimation of winter transport values, and of extreme transports. The data - model comparison in Fig. 12 gives an underestimation of the model of about 10%. But that cannot explain all.

Both shoreward (in the surf zone) and seaward of the TMZ transport will take place as well. Seaward of the TMZ the 20 km wide cross-shore circulation cell as modeled by Visser et al. (1991) will likely also contribute to the northward transport. Although the SPM concentrations in the outer 17 km of this zone are lower than in the TMZ, the residual transport may be still high, as the water depth, and hence the volume of water involved, is larger, and the effect of friction on the currents is weaker when moving further offshore. To provide a speculative estimate: If we assume the transport per meter, found in this study, to linearly decrease to zero in the 17 km wide circulation cell, we obtain a longshore residual transport of 8.5 + 2.5 = 11 Mton/yr, a value that is on the low end of the uncertainty bands. This estimate is of course very uncertain, but it marks that the transport along the Holland coast – and possibly through Dover Strait – may be lower than estimated before. This observation is in agreement with the budget study of Colina Alonso et al. (2024), which assumed a transport volume of 10–14.4 Mton/yr along the Holland coast.

In the surf zone other mechanisms come into play: both the resuspension and the residual current are more strongly influenced by the wave field rather than by the wind-driven and tidal currents as in the TMZ (Grunnet et al., 2005). Supposedly, the residual direction is also northward as in the wave field the SW direction also dominates. But whether the residual transport will be larger, similar or smaller than in the TMZ requires further investigation. The contribution may be low, as this zone is only 0.5 km wide.

One of the limitations of the present study is the lack of precision in the near-bed layer. The lowest OBS sensor at 0.3 m above the seabed has given results that indicate the presence of a fluffy layer close to the seabed (van der Hout et al., 2017). These high concentrations would contribute to the net transport, but on the other hand, near-bed currents are very weak and questions whether the contribution to the overall transport is of significance.

8. Summary and conclusion

In this paper, we analyzed longshore transports of SPM derived from a bottom lander, covering (with some gaps) two years; it was deployed off the coast of Egmond in the Turbidity Maximum Zone (TMZ) fringing the coastline. We exploited the data from an upward looking ADCP moored at the top of the bottom lander to estimate both SPM concentrations and current velocities throughout the water column. The former involves the translation from acoustic backscatter intensity to SPM concentration – generally not straightforward for cohesive sediments –, for which we provided here an adjustment of the standard calibration method by a continuous calibration with the optical backscatter sensors on the lander.

We have split the wind conditions into calm and energetic conditions, with a threshold between the two at a wind speed of 5 m/s. This value corresponds empirically with a wave height of 0.8 m at this site. During calm conditions, no clear effect of wind direction is found on the gross (i.e., in the ebb or flood phase) or net (i.e., tidally integrated) SPM transports. The gross transports are then small, and the net transports are generally northward, irrespective of the wind direction. Large transports during calm conditions may occasionally occur in the aftermath of energetic conditions due to a delayed response of the gross transport to changing conditions. This was analyzed for a particular sequence of storm events. Energetic conditions are characterized by large gross transports due to wave resuspension and enhanced currents. The net transport exhibits a strong asymmetry due to both the predominance of southwesterly winds and the stronger net northward transport for this wind direction, which together induce an annual net northward transport.

The net transport was further studied by applying linear regression to find relations between the net transport and the wind speed from different wind sectors. By extrapolating these findings to a 10-year period (using wind data from weather station IJmuiden as input for the model), a high inter-annual (up to a factor 2) and seasonal variation (up to a factor 5) was found related to the natural variability of the annual wind climate. The extrapolation of the annual mean transport of 1.0 kton/m at the position of the bottom frame to the wider TMZ gives an estimate of 2.5 Mton per year, which is relatively low compared to the average of 22 Mton/yr along the coastline of the Southern Bight. This lower estimate is in line with the recent mud budget study of the Wadden Sea by Colina Alonso et al. (2024) and the numerical model study of Cronin and Blaas (2015). We have also been able to relate the residual transport to the wind climate and tidal currents, with the relative contributions being 2/3 and 1/3, respectively.

The long-term dataset analyzed in this paper reveals the large variability of gross and net SPM transports in individual tidal cycles, highlighting the very importance of having long-term data.

CRediT authorship contribution statement

Carola M. van der Hout: Writing – review & editing, Writing – original draft, Visualization, Methodology, Investigation, Formal analysis, Data curation, Conceptualization. **Rob Witbaard:** Writing – review & editing, Supervision, Resources, Project administration, Methodology, Funding acquisition, Data curation. **Piet Hoekstra:** Writing – review & editing, Supervision, Conceptualization. **Theo Gerkema:** Writing – review & editing, Writing – original draft, Supervision, Project administration, Funding acquisition, Conceptualization.

Declaration of competing interest

The authors declare the following financial interests/personal relationships which may be considered as potential competing interests: Carola van der Hout reports financial support was provided by Rijkswaterstaat Centrale Informatievoorziening. Carola van der Hout, Theo Gerkema, Rob Witbaard reports financial support was provided by Building with Nature. If there are other authors, they declare that they have no known competing financial interests or personal relationships that could have appeared to influence the work reported in this paper.

Acknowledgments

The dataset in this paper has been obtained with the financial support (ref no. LM-006588) of a collaboration between the La Mer Foundation and the Ministry of Infrastructure and Environment (Rijkswaterstaat, The Netherlands) in the project *Monitoring and Evaluation Program Sand mining*. The ADCP was supplied by Deltares within the framework of the research program *Building with Nature*. We thank the crew of the HRMS *Terschelling* and research vessel *Pelagia* for recovering the bottom lander each and every time, which is not that evident. We also thank the crew of research vessel *Navicula* for the stationary measurements. This work has been supported over several years by the research program *Building with Nature* and in the last year by *Rijkswaterstaat*. We thank Leo Maas for his support in the process of forming this article.

Data availability

Data is publicly available via a DOI: https://doi.org/10.25850/nioz/7b.b.ah.

References

Becherer, J., Flöser, G., Umlauf, L., Burchard, H., 2016. Estuarine circulation versus tidal pumping: Sediment transport in a well-mixed tidal inlet. J. Geophys. Res. Ocean. 121, 6251–6270. http://dx.doi.org/10.1002/2016JC011640.

Colina Alonso, A., van Maren, D.S., Oost, P., Esselink, P., Hagen, R., Kösters, F., Bartholdy, J., Bijleveld, A., Wang, Z.B., 2024. A mud budget of the Wadden Sea and its implications for sediment management. Commun. Earth Environ. 153, http://dx.doi.org/10.1038/s43247-024-01315-9.

Cox, J.R., Huismans, Y., Knaake, S.M., Leuven, J.R.F.W., Vellinga, N.E., van der Vegt, M., Hoitink, A.J.F., Kleinhans, M.G., 2021. Anthropogenic effects on the contemporary sediment budget of the lower rhine-Meuse Delta channel network. Earth's Futur. 9, e2020EF001869.

Cronin, K., Blaas, M., 2015. Maasvlakte 2 and Fine Sediment Fluxes Towards the Wadden Sea. Technical Report 1210059-000-ZKS-0005, Deltares.

de Boer, G.J., Pietrzak, J.D., Winterwerp, J.C., 2008. Using the potential energy anomaly equation to investigate tidal straining and advection of stratification in a region of freshwater influence. Ocean Model. 22, 1–11.

de Boer, G.J., Pietrzak, J.D., Winterwerp, J.C., 2009. SST observations of upwelling induced by tidal straining in the Rhine ROFI. Cont. Shelf Res. 29, 263–277. http://dx.doi.org/10.1016/j.csr.2007.06.011.

de Kok, J., 2004. Slibtransport Langs de Nederlandse Kust. Technical Report RIKZ/OS/2004.148w, Ministerie van Verkeer en Waterstaat, The Netherlands.

Deines, K.L., 1999. Backscatter estimation using broadband acoustic Doppler current profilers. In: Proceedings of the IEEE Sixth Working Conference on Current Measurement (Cat. No.99CH36331). pp. 249–253. http://dx.doi.org/10.1109/CCM.1999.755249.

Downing, A., Thorne, D., Vincent, C.E., 1995. Backscattering from a suspension in the near field of a piston transducer. J. Acoust. Soc. Am. 97, 1614–1620.

Duran-Matute, M., Gerkema, T., 2015. Calculating residual flows through a multiple-inlet system: the conundrum of the tidal period. Ocean. Dyn. 65, 1461–1475. http://dx.doi.org/10.1007/s10236-015-0875-1.

Dyer, K.R., Moffat, T.J., 1998. Fluxes of suspended matter in the East Anglian plume Southern North Sea. Cont. Shelf Res. 18, 1311–1331.

Eisma, D., 1987. The North Sea: an overview. Phil. Trans. R. Soc. Lond. B 316, 461–485.

Fettweis, M., Baeye, M., van der Zande, D., van den Eynde, D., Lee, B., 2014. Seasonality of floc strength in the southern North Sea. J. Geophys. Res. Ocean. 119, 1911–1926. http://dx.doi.org/10.1002/2013JC009750.

Fettweis, M., Nechad, B., van den Eynde, D., 2007. An estimate of the suspended particulate matter (SPM) transport in the southern North Sea using SeaWiFS images, in situ measurements and numerical model results. Cont. Shelf Res. 27, 1568–1583. http://dx.doi.org/10.1016/j.csr.2007.01.017.

Fettweis, M., van den Eynde, D., 2003. The mud deposits and the high turbidity in the Belgian–Dutch coastal zone, southern bight of the North Sea. Cont. Shelf Res. 23, 669–691.

Francois, R.E., Garrison, G.R., 1982. Sound absorption based on ocean measurements. Part II : Boric acid contribution and equation for total absorption. J. Acoust. Soc. Am. 72, 1879–1890. http://dx.doi.org/10.1121/1.388673.

Gerkema, T., Duran-Matute, M., 2017. Interannual variability of mean sea level and its sensitivity to wind climate in an inter-tidal basin. Earth Syst. Dyn. 8, 1223–1235. http://dx.doi.org/10.5194/esd-8-1223-2017.

Gostiaux, L., van Haren, H., 2010. Extracting meaningful information from uncalibrated backscattered echo intensity data. J. Atmos. Ocean. Technol. 27, 943–949. http://dx.doi.org/10.1175/2009JTECHO704.1.

Grunnet, N.M., Ruessink, B., Walstra, D.-J.R., 2005. The influence of tides, wind and waves on the redistribution of nourished sediment at Terschelling, The Netherlands. Coast. Eng. 52 (7), 617–631. http://dx.doi.org/10.1016/j.coastaleng.2005.04.001.

Hoitink, A.J.F., Hoekstra, P., 2005. Observations of suspended sediment from ADCP and OBS measurements in a mud-dominated environment. Coast. Eng. 52, 103–118. http://dx.doi.org/10.1016/j.coastaleng.2004.09.005.

Joordens, J.C.A., Souza, A.J., Visser, A., 2001. The influence of tidal straining and wind on suspended matter and phytoplankton distribution in the Rhine outflow region. Cont. Shelf Res. 21, 301–325. http://dx.doi.org/10.1016/S0278-4343(00)00095-9.

Jourdin, F., Tessier, C., Le Hir, P., Verney, R., Lunven, M., Loyer, S., Lusven, A., Filipot, J., 2014. Dual-frequency ADCPs measuring turbidity. Geo-Mar. Lett. 34, 381–397. http://dx.doi.org/10.1007/s00367-014-0366-2.

Kim, Y.H., Voulgaris, G., 2003. Estimation of suspended sediment concentration in estuarine environments using acoustic backscatter from an ADCP. In: Proceedings of Coastal Sediments 2003. vol. 3, pp. 1–10.

Lafite, R., Shimwell, S., Grochowski, N., Dupont, J.P., Nash, L., Salomon, J.C., Cabioch, L., Collins, M., Gao, S., 2007. Suspended particulate matter fluxes through the Straits of Dover, English Channel: observations and modelling. Ocean. Acta 23 (6), 687–700.

McManus, J.P., Prandle, D., 1997. Development of a model to reproduce observed suspended sediment distributions in the southern North Sea using Principal Component Analysis and Multiple Linear Regression. Cont. Shelf Res. 17, 761–778.

Merckelbach, L.M., 2006. A model for high-frequency acoustic Doppler current profiler backscatter from suspended sediment in strong currents. Cont. Shelf Res. 26, 1316–1335.

Otto, L., Zimmerman, J.T.F., Furnes, G.K., Mork, M., Saetre, R., Becker, G., 1990. Review of the physical oceanography of the North Sea. Neth. J. Sea Res. 26, 161–238.

Pietrzak, J.D., de Boer, G.J., Eleveld, M.A., 2011. Mechanisms controlling the intra-annual mesoscale variability of SST and SPM in the southern North Sea. Cont. Shelf Res. 31, 594–610. http://dx.doi.org/10.1016/j.csr.2010.12.014.

Prandle, D., 1978. Monthly-mean residual flows through the Dover Strait, 1949–1972. J. Mar. Biol. Assoc. U.K. 58, 965–973.

Rijnsburger, S., van der Hout, C.M., van Tongeren, O., de Boer, G.J., van Prooijen, B.C., Borst, W.G., Pietrzak, J.D., 2016. Simultaneous measurements of tidal straining and advection at two parallel transects far downstream in the Rhine ROFI. Ocean. Dyn. 66, 719–736. http://dx.doi.org/10.1007/s10236-016-0947-x.

Sahin, C., Verney, R., Sheremet, A., Voulgaris, G., 2017. Acoustic backscatter by suspended cohesive sediments: Field observations, Seine Estuary , France. Cont. Shelf Res. 134, 39–51. http://dx.doi.org/10.1016/j.csr.2017.01.003.

Sassi, M.G., Hoitink, A.J.F., Vermeulen, B., 2012. Impact of sound attenuation by suspended sediment on ADCP backscatter calibrations. Water Resour. Res. 48 (9).

Siegismund, F., Schrum, C., 2001. Decadal changes in the wind forcing over the North Sea. Clim. Res. 18, 39–45. http://dx.doi.org/10.3354/cr018039.

Stanev, E.V., Dobrynin, M., Pleskachevsky, A., Grayek, S., Guenther, H., 2009. Bed shear stress in the southern North Sea as an important driver for suspended sediment dynamics. Ocean. Dyn. 59 (2), 183–194. http://dx.doi.org/10.1007/s10236-008-0171-4.

Thorne, P.D., Hurther, D., 2014. An overview on the use of backscattered sound for measuring suspended particle size and concentration profiles in non-cohesive inorganic sediment transport studies. Cont. Shelf Res. 73, 97–118. http://dx.doi.org/10.1016/j.csr.2013.10.017.

Urick, R.J., 1983. Principles of Underwater Sound. McGraw-Hill.

van Alphen, J.S.L.J., 1990. A mud balance for belgian-dutch coastal waters between 1969–1986. Neth. J. Sea Res. 25, 29–30.

van der Giessen, A., de Ruijter, W.P.M., Borst, J.C., 1990. Three-dimensional current structure in the dutch coastal zone. Neth. J. Sea Res. 25, 45–55.

van der Hout, C.M., Gerkema, T., Nauw, J.J., Ridderinkhof, H., 2015. Observations of a narrow zone of high suspended particulate matter (SPM) concentrations along the dutch coast. Cont. Shelf Res. 95, 27–38. http://dx.doi.org/10.1016/j.csr.2015.01.002.

van der Hout, C.M., Witbaard, R., Bergman, M.J.N., Duineveld, C.G.A., Rozemeijer, M.J.C., Gerkema, T., 2017. The dynamics of suspended particulate matter (SPM) and chlorophyll-a from intratidal to annual time scales in a coastal turbidity maximum. J. Sea Res. 127, 105–118. http://dx.doi.org/10.1016/j.seares.2017.04.011.

van Raaphorst, W., Phillippart, C.J.M., Smit, J.P.C., Dijkstra, F.J., Malschaert, J.F.P., 1998. Distribution of suspended particulate matter in the North Sea as inferred from NOAA/AVHRR reflectance images and in situ observations. J. Sea Res. 39, 197–215. http://dx.doi.org/10.1016/S1385-1101(98)00006-9.

van Veen, J., 1937. Velocities in a vertical line of a stream. Rapporten en mededeelingen van den Rijkswaterstaat, No. 29.

Visser, M., de Ruijter, W.P.M., Postma, L., 1991. The distribution of suspended matter in the Dutch coastal zone. Neth. J. Sea Res. 27, 127–143.

Witbaard, R., Bergman, M.J.N., van Weerlee, E., Duineveld, G.C.A., 2017. An estimation of the effects of ensis directus on the transport and burial of silt in the near-shore Dutch coastal zone of the North Sea. J. Sea Res. 127, 105–118. http://dx.doi.org/10.1016/j.seares.2016.12.001.

Witbaard, R., Duineveld, G.C.A., Bergman, M.J.N., Witte, H.I., Groot, L., Rozemeijer, M.J.C., 2015. The growth and dynamics of ensis directus in the near-shore Dutch coastal zone of the North Sea. J. Sea Res. 95, 95–105. http://dx.doi.org/10.1016/j.seares.2014.09.008.

Yu, Q., Flemming, B.W., Gao, S., 2011. Tide-induced vertical suspended sediment concentration profiles: phase lag and amplitude attenuation. Ocean. Dyn. 61, 403–410. http://dx.doi.org/10.1007/s10236-010-0335-x.